Instantaneous Pressure Reconstruction From PIV In Compressible Launcher Environments

D'Aguanno, A.; Schrijer, F.F.J.; van Oudheusden, B.W.

DOI
10.55037/lxlaser.21st.173

Publication date
2024

Document Version
Final published version

Published in
Proceedings of the 21st International Symposium on the Application of Laser and Imaging Techniques to Fluid Mechanics

Instantaneous Pressure Reconstruction from PIV in Compressible Launcher Environments

A. D'Aguanno[1,*], F.F.J. Schrijer[1], B.W. van Oudheusden[1]
1: Dept. of FPT, Aerodynamics Section, Delft University of Technology
* Correspondent author: A.Daguanno@tudelft.nl

Keywords: Pressure reconstruction, Taylor's hypothesis, PIV, Hammerhead launcher configurations, compressible flows.

ABSTRACT

Modern launcher configurations, often characterized by a larger diameter in the payload fairing than the rest of the launch vehicle (hammerhead configuration), face significant challenges during transonic operations, given their susceptibility to flow separation and intense pressure fluctuations. This experimental study aims to reconstruct pressure from PIV under transonic conditions using Taylor's hypothesis. The focus is on the ESA VEGA-E hammerhead launcher model, investigated in the transonic regime at Ma=0.8 and at α=0°.

Initially, the methodology of the pressure reconstruction algorithm is described and the validity of Taylor's hypothesis is established through validation with numerical data. Subsequently, the experimental data are first used to provide a general characterization of the flow phenomenon, highlighting key features such as an oscillating shockwave, separated and reattached flows. Later, the reconstruction of pressure from velocity data is compared to unsteady pressure transducer data, for instantaneous, average and standard deviation values, obtaining a very good agreement (ΔCp_{Avg}~0.01-0.02 and ΔCp_{Std}~0.02). The experimental set-up is also designed to showcase the impact of neglecting the out-of-plane velocity component on pressure reconstruction, showing comparable data for the average values, while larger discrepancies in terms of standard deviation in particular in the separated area region.

1. Introduction

The effect of unsteady loads exerted on the launcher fairing may be problematic for its structural integrity, the payload and even the stability of the launcher itself. Therefore it is important to understand the sources of the unsteadiness as well as the effects (pressure/loads on the surface). Furthermore, with the need for increased payload volume, launcher fairings become larger in size resulting in so called hammerhead configurations (see Fig 1). For freestream Mach number close to Ma=0.7 local region of supersonic velocity appear with associated shock formation. These shocks interact with the boundary layer developing over the launcher causing flow unsteadiness such as buffet. This effect is increased even more in the rear part of the fairing where the flow tends

to separate. The separation and reattachment of the flow around the model are responsible for the presence of additional flow unsteadiness and associated time varying pressure loads.
In order to experimentally evaluate the unsteady pressures and loads, wind tunnel experiments are needed at representative Reynolds and Mach numbers. Typically these loads can be evaluated through load balances and or unsteady pressure sensors. An example of unsteady pressure sensor measurements is present in *Panda et al.* [1], which highlights the presence of high pressure fluctuations in correspondence of the shockwave structures and in proximity of the reattachment area. Although this method is accurate in determining pressure fluctuations it is affected by the high cost associated with the use of numerous unsteady pressure sensors thus, as an alternative, unsteady pressure sensitive paint (PSP) can be used (see *Schuster et al.* [2]). A drawback of this approach is that only information is provided for the surface pressure without obtaining knowledge on the flow structures that are responsible for them.
In addition, when comparing pressure transducers and PSP data to CFD results, incompatibilities often arise regarding the temporal and spatial sampling of the loads. These significant drawbacks can be remedied by the application of existing particle based flow field measurement techniques to yield not only data on the flow velocity but to provide pressure data as well. This then provides a simultaneous measurement of the flow field and corresponding pressure field.

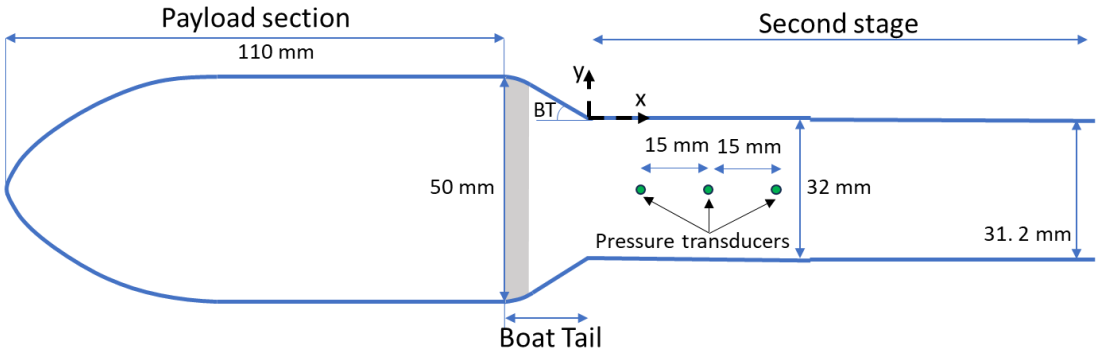

Figure. 1 Sketch of hammerhead VEGA-E launcher model with dimensions.

It has been demonstrated that for incompressible flows it is possible to obtain unsteady pressure from particle image velocimetry (PIV) (see *van Oudheusden* [3] for a review) in turbulent boundary layers, around bluff bodies, inside jets *(Pröbsting et al.* [4]*; de Kat and Ganapathisubramani,* [5]*; McClure and Yarusevych,* [6]) etc. However, the pressure determination is not so straightforward for compressible flows (*van Oudheusden* [7]) and it is still in the development phase. Apart from a variety of technical challenges (tunnel vibrations, limited optical access, short time scales), the fact that the density can no longer be considered as constant has to be accounted for. For the mean pressure field it has been shown that good results can be obtained, under realistic experimental

conditions, for transonic base-flows and shock interactions (*Scharnowski and Kähler* [8]). However in order to obtain pressure fluctuations additional work is needed.

Nowadays the applicability of PIV-pressure reconstruction algorithms in compressible conditions is bounded by technological limitations which limits the laser and camera performance and as a consequence the PIV spatial and temporal resolution. For instance, the camera repetition rate is still generally too low to time resolve the flow field at transonic velocities (see *LaVision* [9]) or to obtain the acceleration field, however it could still be used to time resolve some of the unsteady flow features present in the flow field, such as the shockwave oscillation. A further possibility to extract the acceleration field in an exact manner, is by using a four-pulse system (*Schreyer et al.* [10]). For this specific set-up, two PIV systems are generally used (three systems in *Lynch et al.* [11]), in such a way that couples of correlated velocity fields can be used to compute the acceleration field. However, neither the spectrum for the acceleration field nor for the velocity field can be retrieved. It is also worth stressing that such a set-up is also characterized by being complicated and expensive, since generally the operation of two PIV systems is required.

Furthermore, technical implications or restrictions make time-resolved measurements impractical; thus, Lagrangian and Eulerian approaches for determining the acceleration term (see *van Oudheusden* [3]) are unfeasible. Therefore, a method based on modelling the acceleration term of the momentum equation, seems most attractive for implementation in industrial and compressible environments, notwithstanding its lower accuracy. These approaches are also referred to as single snapshot approach, since the instantaneous pressure is evaluated from information of a single snapshot. In this study, the instantaneous pressure field will be estimated with the Taylor's hypothesis approach (see *de Kat and Ganapathisubramani* [5]).

2. Pressure reconstruction formulation

Sufficiently far away from the launcher model the flow can be considered inviscid and adiabatic, thus the isentropic relations (in combination with the ideal gas law) can be used as boundary conditions for the temperature and the pressure field.

These considerations are not valid in the wake area, where the flow is rotational. However, using the assumption (as a first approximation) that viscous effects are only relevant in the region in close proximity to the model surface, the differential form of the momentum equation allows to obtain the local pressure gradient, as:

$$\nabla p = -\rho \frac{D\boldsymbol{u}}{Dt} + \mu \nabla^2 u \qquad 1$$

The term ρ/p can be derived from the steady, adiabatic energy equation (equivalent to constant total temperature) and from the ideal gas equation (*van Oudheusden et al.,* [12]), yielding to:

$$T = \frac{{V_\infty}^2 + \frac{\gamma-1}{2}{M_\infty}^2\left({V_\infty}^2 - V^2\right)}{\gamma R\, {M_\infty}^2} \quad (2)$$

From which an equation that relates the pressure field to the velocity field is obtained (for adiabatic inviscid flow):

$$\nabla \ln\left(\frac{p}{p_\infty}\right) = -\frac{1}{RT}\cdot\frac{Du}{Dt} = \frac{\gamma\, {M_\infty}^2}{{V_\infty}^2 + \frac{\gamma-1}{2}{M_\infty}^2\left({V_\infty}^2 - V^2\right)}\cdot\frac{Du}{Dt} \quad (3)$$

As previously anticipated in this study, since the exact determination of the acceleration term (Du/Dt) is not feasible, the acceleration term is modelled by means of the Taylor's hypothesis (TH, *de Kat and Ganapathisubramani* [5]*, Laskari et al.* [13]). According to this hypothesis turbulent structures advect in the flow in a "frozen" state, considering that advection due to turbulent circulation is small. Being $\mathbf{U_c}(U_c, V_c, W_c, t)$ the convection velocity of the perturbations and decomposing the velocity field in a mean and a fluctuation component, the following expression is obtained:

$$\frac{Du'}{Dt} = \frac{\partial u'}{\partial t} + (U_c\cdot\nabla)u' = 0 \rightarrow \frac{\partial u'}{\partial t} = -(U_c\cdot\nabla)u' \quad (4)$$

Under these hypothesis it is possible to retrieve time information on the base of spatial information obtaining the following expression for the pressure gradient:

$$\nabla \ln\left(\frac{p_{TH}}{p_\infty}\right) = -\frac{1}{RT}\cdot\frac{Du}{Dt} = \frac{\gamma\, {M_\infty}^2}{{V_\infty}^2 + \frac{\gamma-1}{2}{M_\infty}^2\left({V_\infty}^2 - V^2\right)}\cdot\left(-(U_c\cdot\nabla)u' + u\cdot\nabla u\right) \quad (5)$$

de Kat and Ganapathisubramani [5] showed that the TH works for flows where turbulent fluctuations are small and thus generally the associated error is higher for strongly turbulent and separated flows. The convection velocity of the turbulent structures is generally well approximated by the mean velocity (*Laskari et al.* [13] and *van Gent et al.* [14]). However, this assumption is generally not valid in presence of a shear layer as documented by *Lin* [15] and *Davoust and Jacquin* [16] among the others. TH has been first successfully applied to volumetric data (*de Kat and Ganapathisubramani* [5]) and more recently to 2D planar PIV data, like in the study of *Van der Kindere et al.* [17]. With the 2D assumption an error of about 5-10% is introduced with respect to the 3D case for the instantaneous field, differently only non-relevant discrepancies affects the mean pressure reconstruction. Furthermore, in the latter study, the Taylor's hypothesis approach showed good agreement with 2D Eulerian data or 2D (pseudo-)lagrangian data, with a smother p_{rms} (pressure rms) profile and more robust to measurement noise. This is not surprising since the

Eulerian and the Lagrangian approaches are affected by noise on both the spatial and temporal gradients, differently the TH is only sensitive to noise on the spatial information.
In this study only 2D planar and stereo particle image velocimetry (PIV) measurements will be taken into account, in view of the complexity of volumetric PIV experiments). Therefore, neglecting the out of plane derivatives the following simplified equations are obtained:

$$\frac{\partial}{\partial x}\ln\left(\frac{p_{TH}}{p_\infty}\right) = \frac{\gamma\, {M_\infty}^2}{{V_\infty}^2+\frac{\gamma-1}{2}{M_\infty}^2\left({V_\infty}^2-V^2\right)}\cdot\left(-U_c\frac{\partial u'}{\partial x}-V_c\frac{\partial u'}{\partial y}+u\frac{\partial u}{\partial x}+v\frac{\partial u}{\partial y}\right) \quad 6$$

$$\frac{\partial}{\partial y}\ln\left(\frac{p_{TH}}{p_\infty}\right) = \frac{\gamma\, {M_\infty}^2}{{V_\infty}^2+\frac{\gamma-1}{2}{M_\infty}^2\left({V_\infty}^2-V^2\right)}\cdot\left(-U_c\frac{\partial v'}{\partial x}-V_c\frac{\partial v'}{\partial y}+u\frac{\partial v}{\partial x}+v\frac{\partial v}{\partial y}\right) \quad 7$$

It is worth mentioning that in the case of stereo PIV measurements, three velocity component are retrieved in the measurement plane, therefore the square of the velocity magnitude is evaluated as $V^2 = u^2 + v^2 + w^2$.
From the equations 6, 7 the pressure field can be obtained either with spatial integration or by solving the respective Poisson equation.
In *Souverein et al.* [18], the shockwave was first localized by means of the divergence field and then the shockwave is treated separately by applying shock relations. In the remaining FOV the previous relation is applied. In a further study, *van Oudheusden* [7] showed that this spatial integration procedure could also be applied across a shockwave when using a conservative formulation of the momentum equation. The validity of the inviscid flow assumption is based on the fact that for high Reynolds number applications, the lengths scale associated with viscous phenomena are small and therefore have a non-relevant contribution in the spatial integration of the pressure gradient, see for example *Murai et al.* [19].
In this study the pressure field is computed by solving a Poisson equation (see *Charonko et al.* [20], *de Kat and van Oudheusden,* [21]) which is obtained by applying the divergence to the (logarithm of the) pressure gradient:

$$\nabla\cdot\nabla\ln\left(\frac{p_{TH}}{p_\infty}\right) = \nabla^2\left(\ln\left(\frac{p_{TH}}{p_\infty}\right)\right) = \frac{\partial^2}{\partial x^2}\left(\ln\left(\frac{p_{TH}}{p_\infty}\right)\right)+\frac{\partial^2}{\partial y^2}\left(\ln\left(\frac{p_{TH}}{p_\infty}\right)\right) \quad 8$$

The choice of this pressure determination is associated with the fact that the spatial marching (integration) methods bring to higher errors (is less robust) in presence of velocity errors with respect to the Poisson approach (see *McClure and Yarusevich* [22]).
To solve the Poisson equation, Neumann boundary conditions are imposed on all sides except on the top surface of the domain (see Fig. 2) where the isentropic pressure value is used as a Dirichlet boundary condition. In this study, the Poisson equation is solved with the same approach of *Ragni*

et al. [23] and therefore, discretizing the Poisson equation with a second order finite difference scheme and then, inverting a linear system of equations.

In terms of discretization, the spatial derivatives are obtained with a central difference scheme in the internal points and forward and backward scheme at the boundaries.

It is worth mentioning that although the Taylor's hypothesis approach has been successfully applied to subsonic experimental data and compressible volumetric synthetic data (*van Gent et al.* [14]), such an approach has never been applied to experimental compressible velocity data.

3. Methodology

3.1 Experimental investigation

The current experimental study was accomplished in the transonic-supersonic wind tunnel (TST 27) of TU Delft, which is a blowdown wind tunnel with a test section that is 25.5 cm high and 28 cm wide. The experiments were conducted with a total pressure p_0=2 bars, total temperature T_0=288 K and a Mach number Ma = 0.80.

The experimental model which has been tested is the ESA launcher VEGA-E, which is characterized by an ogive nose, curved edges (grey region in Fig. 1) in the payload-boat tail junction, and a conical boat tail with a 30° inclination. Figure 1 depicts a schematic of this model, including characteristic dimensions. The model has been tested for α=0° and has a payload diameter D=50 mm and a second-stage diameter d=32 mm, resulting in a step height h=(D−d)/2=9 mm. It is worth mentioning that this configuration bears similarity to the well-known *Coe and Nute* ([24]) configuration (BT=34°), for which a large dataset for transonic Mach numbers (particularly for Ma=0.8 and α=0-4°) is available.

The model was also equipped with three unsteady pressure (Endevco Model 8507C) transducers which are localized 25, 55, 85%D downstream of the boat tail bottom corner. These sensors are used to locally validate the pressure data obtained from the PIV measurements.

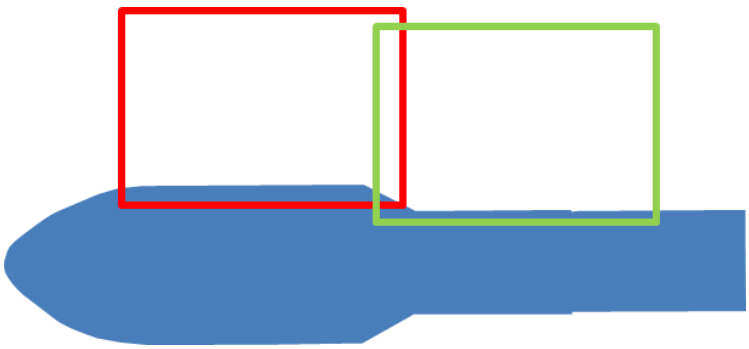

Figure. 2 Side view of PIV field of views.

To ensure a fully turbulent boundary layer over the launcher model, a transition trip was added at 20% of the nose length. This position corresponds to approximately 5% of the entire model length, a location suggested by Goin and Pope [25]. In this study, the transition trip consists of a strip of 1 mm of width (0.11 mm of thickness) with carborundum particles attached on it (particle size of 0.0139 mm).

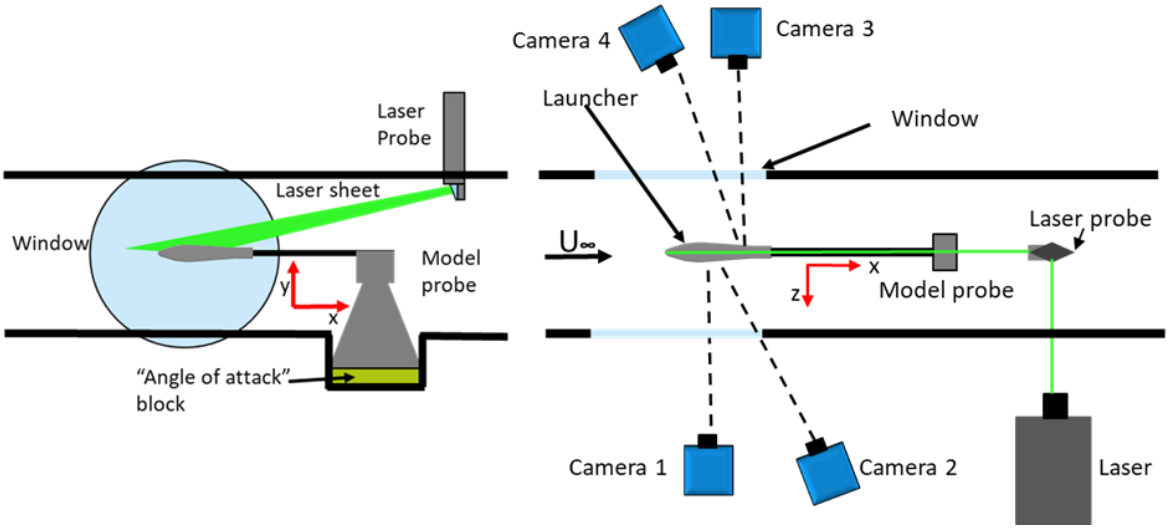

Figure. 3 Side (left) and top view (right) of PIV set-up.

For the PIV measurements, four LaVision sCMOS 5MP cameras (resolution 2560 x 2160 pixels) were used and fitted with 105 mm lenses with an f-stop of 8, acquiring a total number of 1000 images per camera. The cameras were operated in double pulse mode with pulse separation $\Delta t=3\mu s$ and were set in stereo-PIV configuration. The cameras were divided into two groups to visualize two overlapping FOVs (see Fig. 2). In each camera group, one of the two cameras had a planar orientation, and a second one was inclined of 30° with respect to the FOV, requiring the use of a Scheimpflug. This configuration was chosen to facilitate the comparison of pressure reconstruction results between planar PIV and the reconstruction obtained with stereo-PIV data (which also captures the out-of-plane component, but not the velocity gradients). The camera resolution resulted in a combined field of view in the chordwise-vertical plane which is 20 cm long and 5 cm high. Two cameras have been centered in the nose area and the remaining two in correspondence of the boat tail and reattachment region to ensure a visualization of the shockwaves, the separated area and the reattachment location (see all the PIV settings in Table 1).

The seeding particles consist of DEHS droplets, which have a relaxation time of 2µs. These particles were illuminated in a 1mm thick light sheet by a dual cavity laser (Quantel Evergreen 200 laser) with a repetition frequency of 15 Hz. The laser beam is inserted in the wind tunnel by means of a

laser probe, which had access from the top wall of the wind tunnel (see Fig. 3, left). To ensure a synchronization between cameras and laser, a LaVision programmable time unit was employed.
Once the PIV images were collected in Davis 10.0.5, they were first pre-processed in the same software using a Butterworth filter (with a kernel of 7 images, as suggested by *Sciacchitano and Scarano* [26]) to reduce laser reflections and maximize the signal-to-noise ratio. The velocity field was then extracted using stereo and planar cross-correlation. In both cases, a multi-pass approach was chosen, starting with 2 passes with a window size of 96x96 pixels and three subsequent steps with a circular window size of 48x48 pixels. A window overlap of 75% resulted in a vector spacing of 0.9% of the diameter of the model (0.45 mm). Finally, the universal outlier detection with a threshold value of 2 was utilized to eliminate outliers. Further processing, including the pressure reconstruction, was completed in Matlab. The main PIV settings are summarized in Table 1.
This PIV procedure is associated with various sources of uncertainty. For example, the cross-correlation procedure has an uncertainty lower than 0.1 pixels, which results in a corresponding uncertainty on the velocity lower than 1.5 m/s. Additionally, the velocity estimation is affected by the relaxation time of the seeding particles (2 µs for DEHS, see *Ragni et al.* [27]). This effect can cause local uncertainty values as high as 50 m/s in the vicinity of shockwaves; however, this uncertainty is negligible in the remaining part of the FOV.

Table. 1 Settings of PIV experiment and synthetic data-set.

Parameter	PIV experiment	Synthetic PIV data-set
Mach number	0.8	0.7
Model diameter (D)	50 mm	50 mm
Step height (h)	9 mm	15 mm
Camera	4 x sCMOS 5MP	4 x virtual camera
Lenses	105 mm	75 mm (virtual)
Acquisition frequency	15 Hz	500 kHz
Number of images per test case	1000	41
Combined resolution	4500 x 1800 pix	1624 x 800 pix
Pulse separation	3 µs	2 µs
Combined field of view	200 mm x 50 mm	60 mm x 24 mm x 4 mm
PIV configuration	2x stereo/ 2x planar	1x Tomo
Final window size	32 x 32 pix	32 vox
Window overlap	75%	75%
Vector spacing	0.45 mm	0.35 mm

3.2 Synthetic data-set

To validate the methodology described in Section 2, synthetic PIV data from the numerical simulations of *van Gent et al.* [14] have been used. The flow geometry of this synthetic experiment consists of an axisymmetric step, which is representative of the flow over the base of a launcher in the ascent phase. Thus, this data is well suited for validating the pressure reconstruction approach for launcher applications.

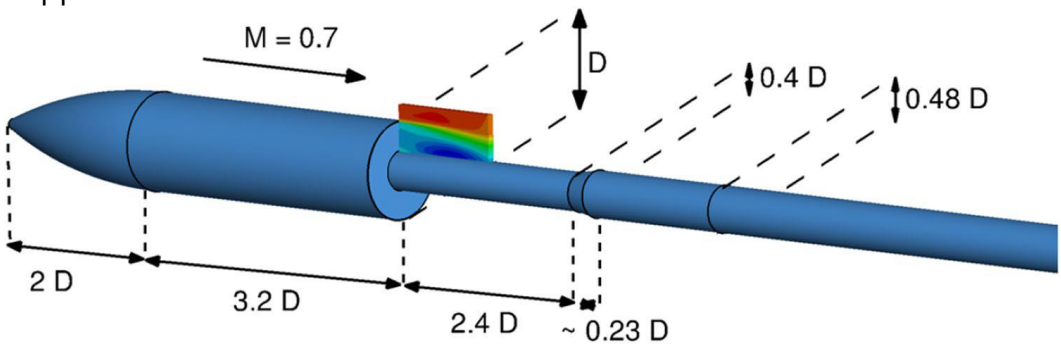

Figure. 4 Sketch of the model geometry of the synthetic PIV experiment with field of view (FOV). Image from *van Gent et al.* [14].

Figure 4 shows the model geometry, and the virtual measurement volume of the synthetic experiment. The model has a forebody with a diameter (D) of 50 mm and an afterbody diameter (d=0.4D) of 20 mm, as a result, the axisymmetric step height is 15 mm. These dimensions are similar to the experimental model investigated in this study (see Table 1, where also other characteristic information are summarized). The freestream Mach number (M_∞) is 0.7, the total pressure (p_0) is 200 000 Pa and the total temperature (T_0) 285 K. In view of the availability of the synthetic data, for this case the pressure reconstruction strategies are not bounded by technological limitations, therefore the pressure reconstruction obtained with the Taylor's hypothesis has been compared to an ideal Eulerian time-resolved pressure reconstruction method (TR) (see *van Oudheusden* [3]).
Although the synthetic data were obtained in a volume (60 mm × 24 mm × 4 mm) with Tomo-PIV processing, only the three velocity components in the central measurement plane (z=0) have been considered to replicate the same typology of (stereo-) data obtained from the experimental campaign. The final FOV of the synthetic PIV data is restricted to just downstream of the background-facing step geometry, and the data have a similar spatial resolution (0.35 mm) as the actual PIV experiment.

4. Validation with synthetic data

In Fig. 5 the instantaneous pressure field is shown for the reference, TH and TR data. The general shape of the pressure coefficient is well recovered by the TH approach, however the magnitude of

the min and the max of Cp are not perfectly recovered. As expected, a better agreement is instead obtained with the TR approach.

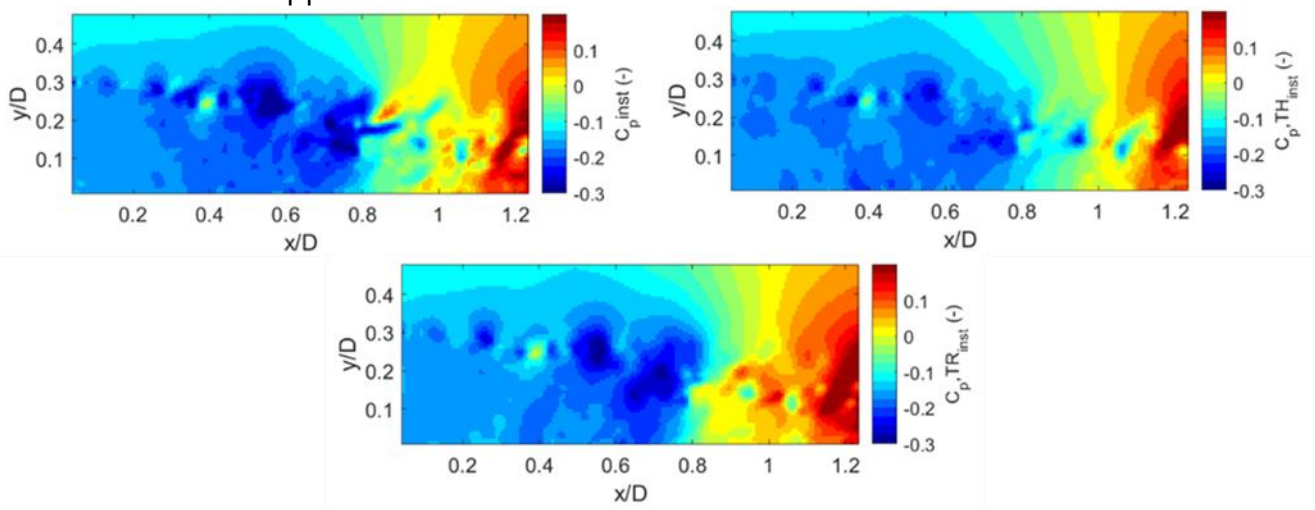

Figure. 5 Instantaneous static pressure coefficient for reference data (top left), Taylor's hypothesis approach (top right) and time-resolved approach (bottom).

To better estimate the behavior of the TH approach, the error field (not shown here for brevity) defined as $E=C_{p,TH}-C_p$ is computed, obtaining a maximum errors in the order of |E|=0.1 in the shear layer region where the convection velocity is supposed to differ the most from the average velocity value. In most of the remaining areas of the FOV a remarkable agreement is present, with |E|<0.03. The comparison of the average pressure coefficient (Fig. 6) confirms the good capability of the TH approach in estimating mean pressure, with similar accuracy also obtained for the TR approach. The comparison of the figures confirms the slightly lower accuracy in the shear layer region, with error lower than 5% in the remaining FOV.

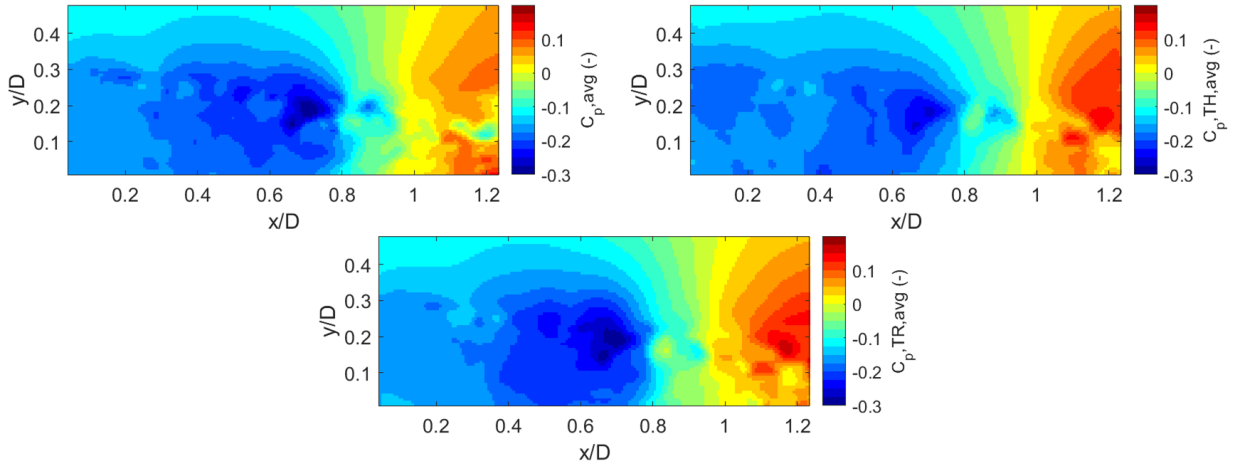

Figure. 6 Average static pressure coefficient for reference data (top left), Taylor's hypothesis approach (top right) and time-resolved approach (bottom).

The standard deviation of the Cp field in Fig. 7 confirms the capability of the TH approach in predicting pressure fluctuations. Surprisingly, lower accuracy is obtained with the TR approach, which in this restricted data set (41 snapshots) appears to overpredict the extent of the region with significant fluctuations. These results align with the findings of *van Gent et al.* [14], who used the same data set to compare different pressure reconstruction strategies. However, it is worth noting that the latter study utilized volumetric data, thereby accounting for out-of-plane gradients.

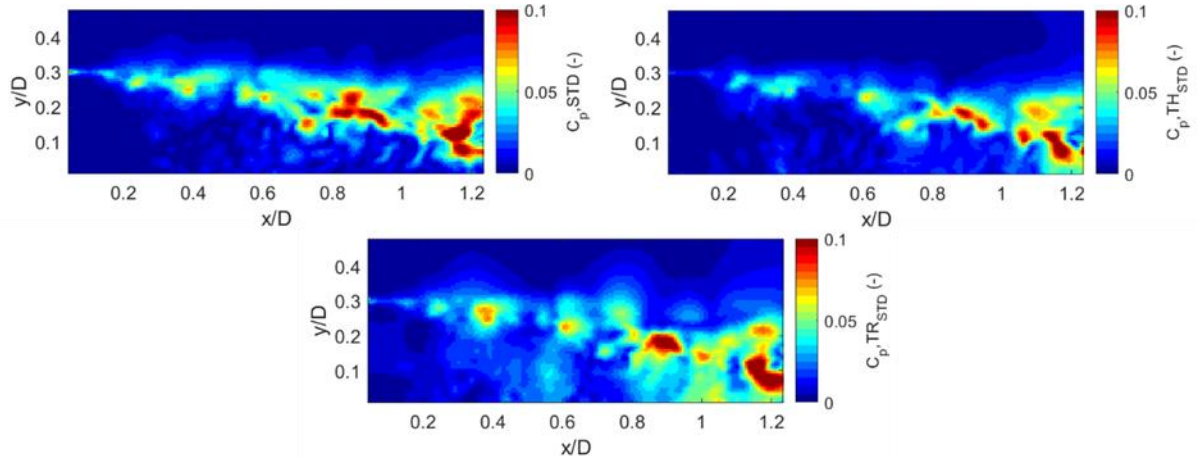

Figure. 7 Standard deviation of pressure coefficient for reference data (top left), Taylor's hypothesis approach (top right) and time-resolved approach (bottom).

5. Pressure transducers data

Before delving into the PIV results, some features of the pressure transducer measurements are here discussed. The pressure measurements were conducted simultaneously with the PIV measurements. However, the pressure transducers feature a much higher acquisition frequency (50 kHz). To synchronize the PIV images with the pressure transducer measurements accurately, the triggering signal of the first laser pulse was recorded by a LabView program along with the signal of the pressure transducer. This allowed for obtaining the value of the pressure transducer at the same time-step as when the PIV images were acquired.

For example, in Fig. 8, the time variation of the first pressure transducer (x/D=0.25) from the start-up to the shut-down of the wind tunnel is depicted by the blue line. Additionally, the values of the pressure transducers at the instant when the PIV images were acquired are marked in red (* in the figure). The main statistical values (mean and standard deviation) of the different pressure transducers will be discussed in conjunction with the analysis of the PIV data in Section 6.

The entire dataset of pressure measurements (excluding the start-up and shut-down phases of the wind tunnel) was utilized for correlation analysis, leveraging the high acquisition frequency of the

transducers. In Fig. 9 (left), the autocorrelation of the three pressure transducers is illustrated. Besides the prominent peak for τ=0 ms, no significant peak can be easily discerned, indicating that the spectrum is not dominated by just one tonal contribution.

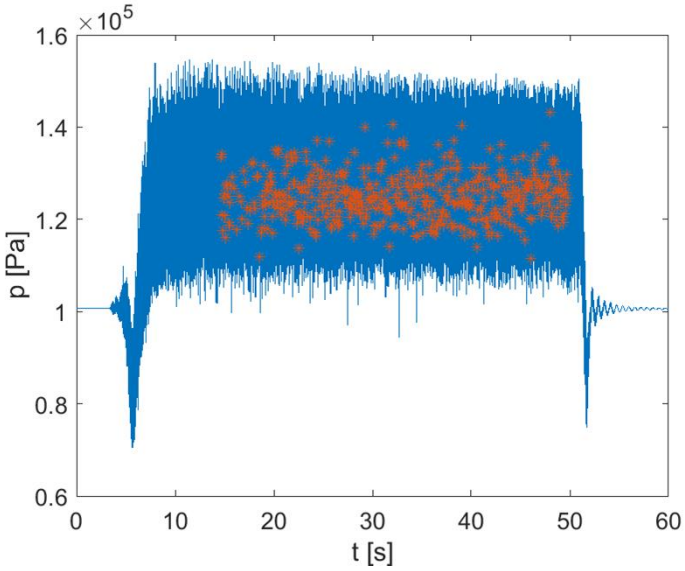

Figure. 8 Time behavior of first pressure transducer for launcher model with Ma=0.8 and α=0°. The red markers indicate the pressure acquisition simultaneous to PIV snapshots acquisition.

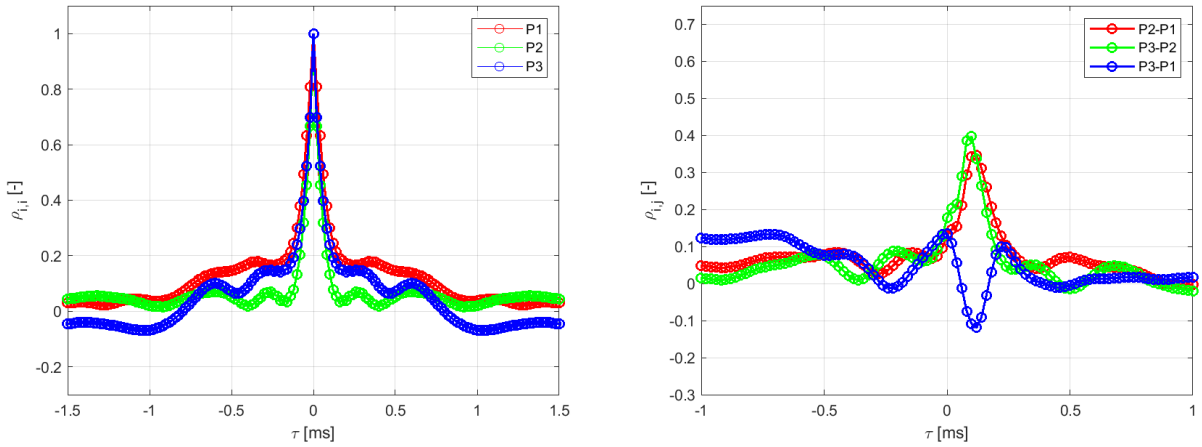

Figure. 9 Autocorrelation (left) and cross-correlation (right) of all pressure transducers for launcher model with Ma=0.8 and α=0°.

On the contrary, in Fig. 9 (right), the cross-correlation of the pressure signals from different transducers is presented. All cross-correlations exhibit non-negligible correlation peaks, particularly the ones between consecutive pressure transducers: p_2-p_1 (cross-correlation between the pressure signals of the second and first pressure transducers) and p_3-p_1 (cross-correlation between the pressure signals of the third and second pressure transducers). The red line (p_2-p_1) displays a peak at τ=0.12 ms, indicating that structures passing through the first pressure

transducer at time step t_0 will reach the second pressure transducer at $t=t_0+0.12$ ms. Considering a distance of 15 mm between the transducers, this is consistent with a convection velocity of 125 m/s. For the green line, the peak of the cross-correlation is taking place at a slightly lower value of τ, $\tau=0.10$ ms, which corresponds to a convection velocity of 150 m/s.
At approximately the same time delay, the blue curve, representing the cross-correlation between the third and first pressure transducers, exhibits anti-correlation, indicative of the shedding of vortex of opposite sign, which are approximately equispaced.

6. PIV-based pressure field

6.1. Instantaneous field

At first the capacity of the pressure reconstruction algorithm to generate pressure fields is here discussed for instantaneous snapshots. The relative instantaneous velocity field is depicted for the three velocity components in Fig. 10, highlighting key flow features. In the nose area, an expansion of the flow occurs, reaching locally supersonic velocities (see U_{inst} in Fig. 10, top left). As the flow approaches the cylindrical portion of the fairing, a quasi-normal shockwave is formed. Positive vertical velocity is observed in the nose area for the vertical velocity component (V_{inst}). Conversely, the out-of-plane velocity component (W_{inst}) exhibits significant velocity upstream of the shockwave and within the shockwave oscillation range, attributed to aberration effects, particularly prominent in shockwaves and expansion regions.

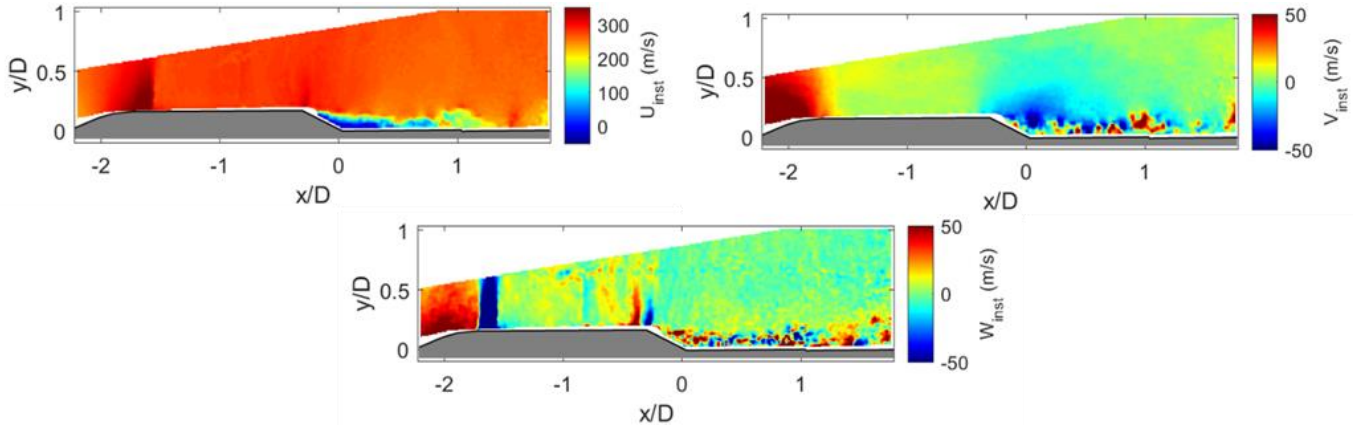

Figure. 10 PIV average velocity field for Ma=0.8, α=0°. On the left streamwise velocity component, on the right vertical velocity component.

Upon reaching the boat tail, a small secondary supersonic area is visualized, accompanied by aberration effects in the out-of-plane velocity component. The streamwise velocity component

illustrates the presence of a separated and recirculation region, extending less than a diameter downstream of the boat tail trailing edge. The boat tail geometry induces a negative vertical velocity and the shedding of vortices, vividly depicted by both the vertical and out-of-plane velocity components.

The streamwise component of the material derivative, in Fig. 11 (obtained applying Eq. 4), reveals distinct flow structures corresponding to expansion (positive values due to flow acceleration) and compression regions (negative values). Similar regions are observed for the vertical component as well. Both material derivative components also clearly depict high acceleration values corresponding to the vortex structures in the separated area.

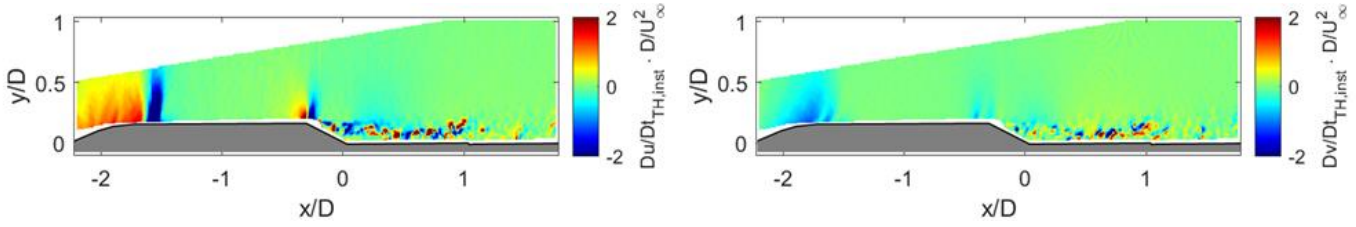

Figure. 11 Instantaneous material derivative for Ma=0.8, α=0° for streamwise (left) and vertical (right) components.

The pressure coefficient field in Fig. 12 (obtained solving the Poisson equation, Eq. 8), displays negative values in the nose area due to the expansion region. As expected, a steep positive jump in pressure is observed across the adjacent shockwave structure. A second expansion region is also observed just upstream of the boat tail, in agreement with Fig. 10. Further downstream, the effect of vortex shedding can also be observed on the pressure field, with the highest pressure region experienced near the reattachment location. More details about these flow features will be provided in the next sub-section, along with the mean and standard deviation values.

To demonstrate the agreement between the reconstructed pressure from the algorithm and the pressure values on the surface of the launcher model, Fig. 12 (right) depicts the pressure profile for x/D=0.25, x/D=0.55, and x/D=0.85, corresponding to the three unsteady pressure transducers locations. The figure illustrates a very good agreement between the instantaneous PIV-based pressure profiles and the values from the pressure transducers (due to a malfunction of the second pressure transducer, it was only possible to retrieve pressure fluctuations from this transducer and not the average value). Part of the difference in pressure value between the PIV-based method and the transducers is attributed to the fact that PIV measurements cannot directly recover the pressure on the surface of the model due to laser reflections and the computation of velocity gradients. For instance, an extrapolation of the pressure profile (not directly shown) on the launcher surface aligns even better with the values shown by the pressure transducer.

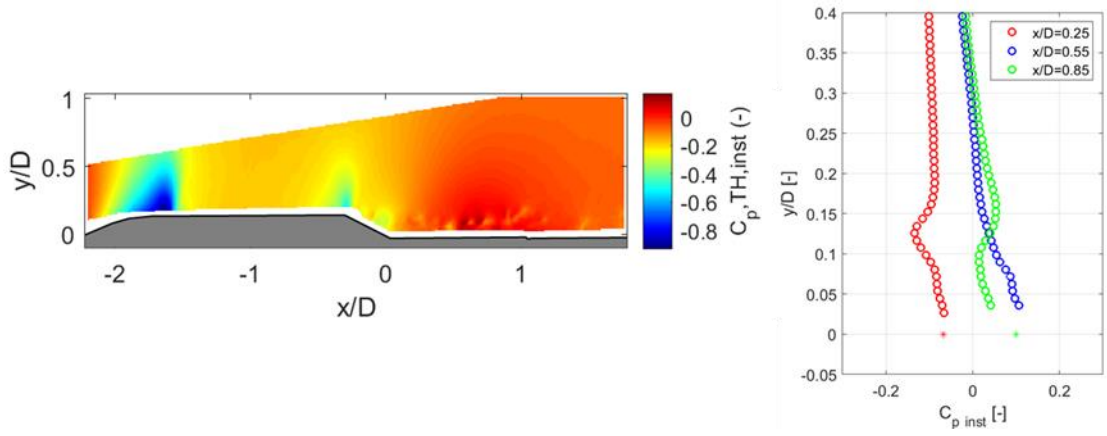

Figure. 12 Instantaneous pressure coefficient (left) and relative profiles in correspondence of pressure transducers for Ma=0.8, α=0°. For y/D=0, the pressure values obtained from the unsteady transducers are indicated with "*".

6.2. Flow field statistics

The average velocity field (Fig. 13) reveals the main flow features discussed for the instantaneous velocity field. Specifically, there is a local supersonic area in the last part of the nose cone, followed by a shockwave with an average position at x/D=-1.7D.

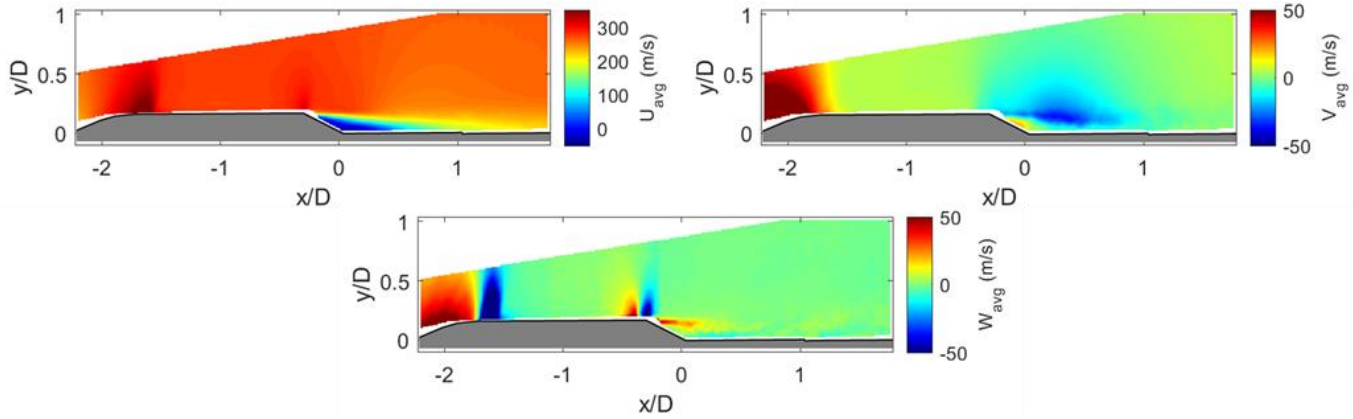

Figure. 13 Average velocity field for Ma=0.8, α=0° for streamwise (top-left), vertical (top-right) and out of plane (bottom) components.

On average, the second supersonic area is barely visible, with a low dissipative shockwave just downstream. The figure demonstrates that the field of view (FOV) fully characterizes the entire separated area and the average reattachment location, occurring at $x_{reat}/D=0.31$. It's important to note that the reattachment location is referenced with respect to the boat tail bottom corner, which does not align with the separation length. The separation initiates along the boat tail, with the total separation length (Δx_{sep}) of 0.50 D, or 2.8 h (step height of 9 mm). This value of separation length is lower than the value reported in literature for the Coe and Nute configuration (86%D in

D'Aguanno et al. [28]), or of a BFS case (~D as documented by *Schrijer et al.* [29] and *Hudy et al.* [30]). This discrepancy is expected to be associated with the smooth boat tail corners which characterize the VEGA-E model, with respect to the sharp geometric transition of the Coe and Nute model.

The vertical velocity field emphasizes a positive vertical velocity in the nose area. A similar positive velocity can be observed in the boat tail area near the launcher's surface, confirming the presence of a recirculation area. Downstream of the boat tail corner, a negative vertical velocity is observed due to the boat tail geometry. The out-of-plane velocity component indicates zero velocities in the entire FOVs except for expansion, compression, and the first part of the shear layer.

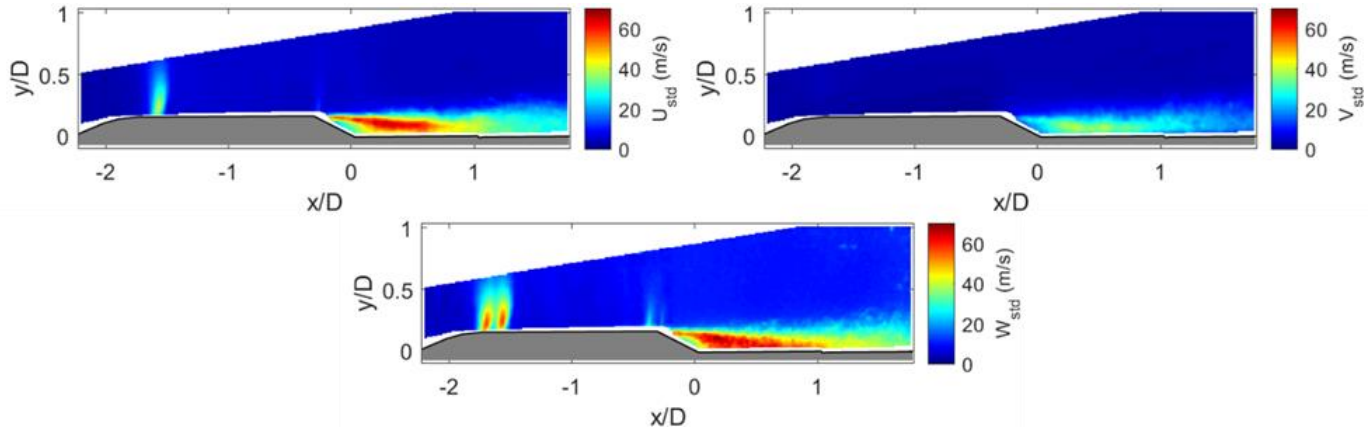

Figure. 14 Standard deviation field for Ma=0.8, α=0° for streamwise (top-left), vertical (top-right) and out of plane (bottom) components.

To better visualize the dynamics of the velocity field, the fluctuations of the three velocity components are depicted in Fig. 14. Both the streamwise and out-of-plane velocity components exhibit significant fluctuations corresponding to the first shockwave structure. Similar fluctuations are not observed for the vertical velocity component. Fluctuations in the secondary shockwave structure are barely visible in the standard deviation fields of the streamwise and out-of-plane velocity components, indicating the lower strength of this shockwave and its almost fixed location. However, all the velocity components highlight a high level of unsteadiness in the shear layer and in the separated area. It is interesting to note that the level of fluctuations is negligible in the region of the FOV directly in contact with the boat tail, suggesting that a steady recirculation bubble occurs in this area. The high level of fluctuations of the out-of-plane velocity component justifies a more detailed analysis of the effect of considering the out-of-plane velocity component for pressure reconstruction. This analysis will be discussed in Section 6.3.

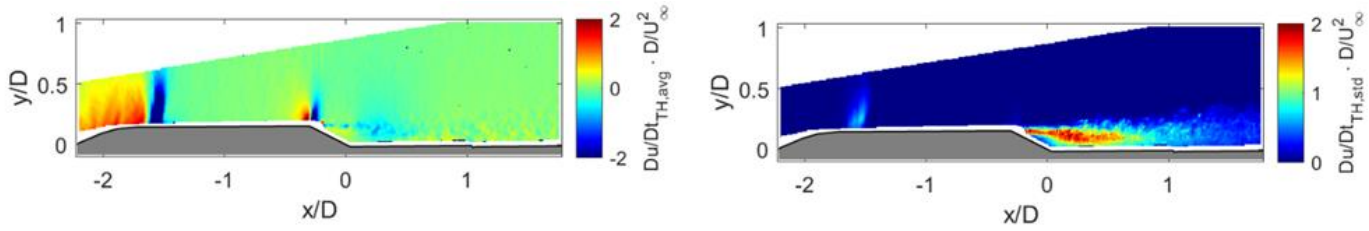

Figure. 15 Material derivative field for Ma=0.8, α=0° for streamwise (left), vertical (right) components.

Regarding the material derivative, in Fig. 15, the average and standard deviation of the streamwise velocity component are displayed, highlighting negative average values in correspondence with the shockwave structure, while as expected positive values occur in the expansion areas. Regarding the fluctuation term, high values are obtained in correspondence with the oscillation range of the first shockwave and in the separated region.

The corresponding average pressure field (obtained by averaging all the instantaneous pressure snapshots) is shown in Fig. 16 (left) and exhibits a similar shape to the instantaneous field, with main contributions in the supersonic area, the two shockwave structures, and in the reattachment region. Considering the standard deviation of the pressure coefficient (Fig. 16, right), the main pressure fluctuations appear in the shockwave range and in the separated area.

It is interesting to note that while for the material derivative, the fluctuations have the highest intensity in the shear layer, in a region slightly detached from the model surface (red region vs green region in Fig. 15, right for x/D=0.4), for the pressure field, the largest fluctuations are actually experienced at the surface of the launcher. Therefore, it should be taken into account that the level of pressure fluctuations on the model surface could be underestimated by the values observed at the bottom of the FOV, due to the lack of information in the region directly in contact with the model surface.

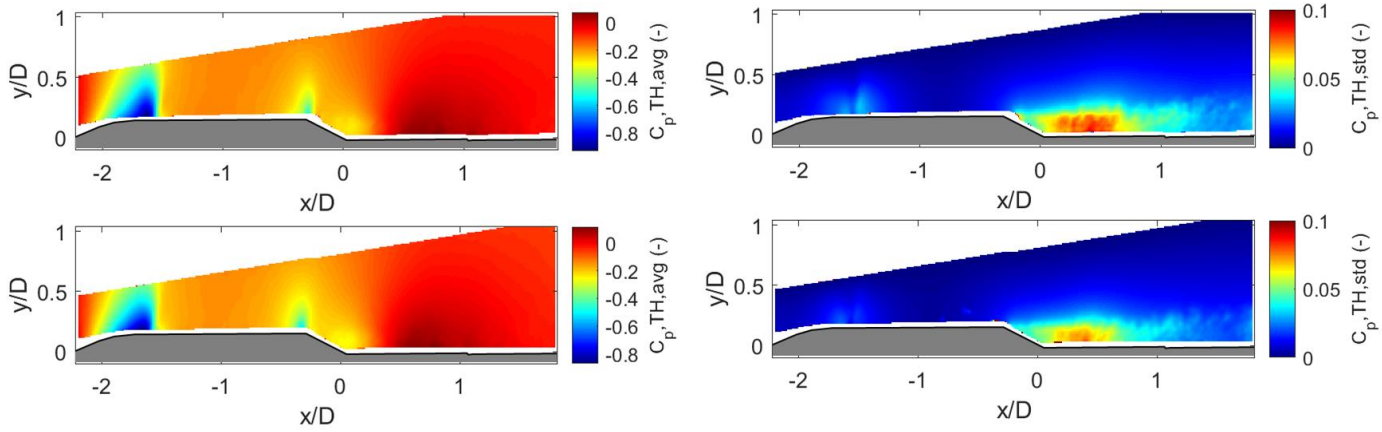

Figure. 16 Mean pressure coefficient (left) and relative standard deviation (right) fields for, Ma=0.8, α=0 for stereo-PIV (top) and planar-PIV data (bottom).

To better appreciate the accuracy of the pressure reconstruction procedure on the main statistics, the profiles of both the average pressure field and the standard deviation are shown in Fig. 17 for the streamwise locations where the unsteady pressure transducers are located (x/D=0.25, 0.55, 0.85). For better understanding of these profiles, the relative streamwise velocity profiles are also reported in Fig. 18.

Lower values of pressure coefficient are obtained at the most upstream streamwise location, where, as shown in Fig. 13, a region of reverse flow is still present. More downstream, very similar pressure profiles are obtained for the two configurations, although some relevant discrepancies are present in terms of shear layer thickness in the velocity profile. The average pressure values at the surface (from pressure transducers) are in excellent agreement with those reconstructed from the velocity data.

In terms of pressure fluctuations, higher values are evident for the two most upstream locations. This is associated with the fact that the first two pressure transducers are located in the region of oscillation of the instantaneous reattachment location, which is also associated with the highest velocity fluctuations, as depicted in Fig. 18.

It is also worth mentioning that there is a certain underestimation of the pressure fluctuations from the velocity-based method, with the difference being smaller for x/D=0.25 and x/D=0.55, while more significant for the most downstream location. This difference is expected to be mainly associated with the lack of velocity information rather than inaccuracy errors of the proposed pressure estimation procedure. For instance, at the most downstream locations, the shear layer thickness is relatively small, and the associated high-energy fluctuations are taking place in a region that is partly not retrieved from the selected FOV due to laser reflections, etc. Conversely, for the case in which the pressure transducers are fully immersed in the separated region, the level of unsteadiness at the bottom of the FOV is already comparable with that measured by the pressure transducers at the model surface. In Fig. 18 (right), the velocity profiles are also shown at the mid-point of consecutive transducers (x/D=0.40 and x/D=0.70). Based on one of the hypothesis of this study ($U_{conv}=U_{Avg}$) these profiles are indicative of the convection velocity of flow structures between pressure transducers, which was computed by the cross-correlation of the pressure data shown in Fig. 9 (right). The mean velocity profile at x/D=0.70 agrees well with the computed convection velocity from the pressure transducer data (150 m/s). However, the discrepancy is larger for x/D=0.40, where the expected convection velocity is 125 m/s. This result is not surprising, as that region is fully immersed in the separated area, therefore, there the assumption that the mean velocity is equivalent to the convection velocity is the least accurate.

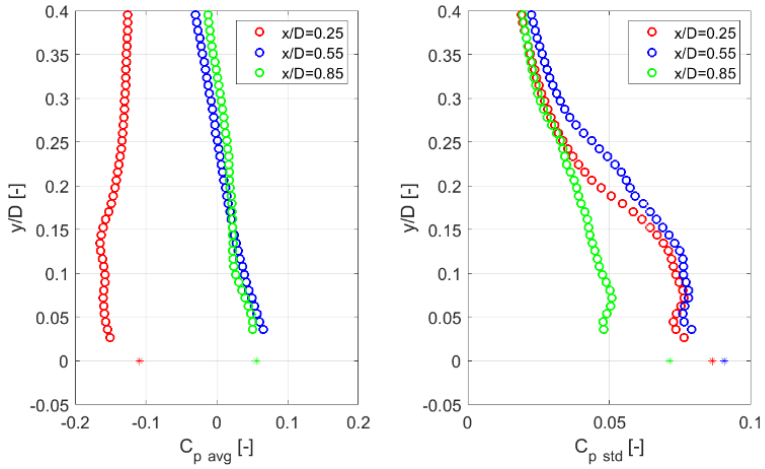

Figure. 17 Mean (left) and standard deviation (right) of the pressure coefficient profiles in correspondence of pressure transducers for Ma=0.8, α=0°.

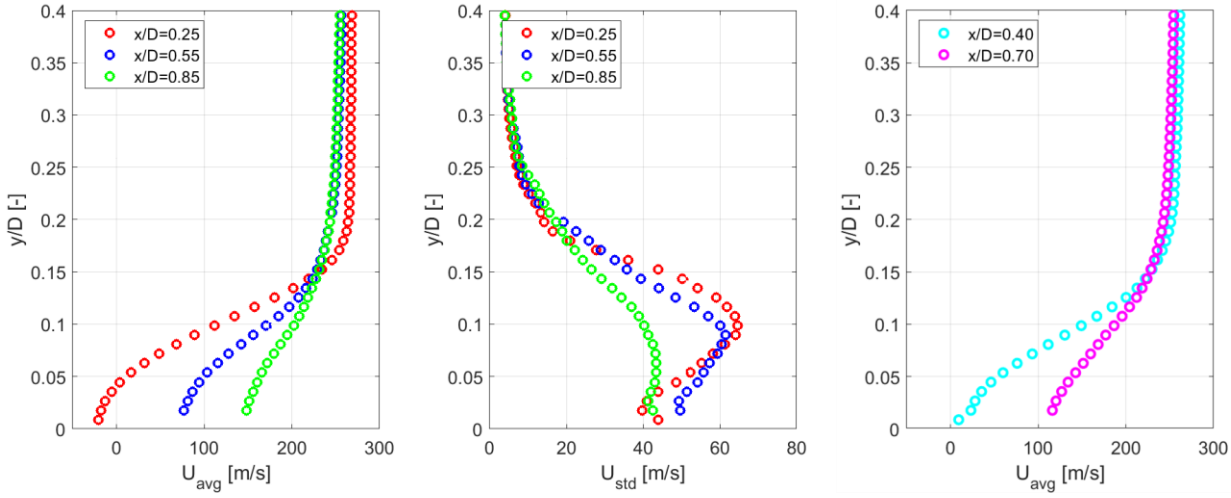

Figure. 18 Mean (left) and standard deviation (center) of the streamwise velocity profiles in correspondence of pressure transducers for Ma=0.8, α=0°. On the right, the velocity profiles are also shown for x/D=0.40 and x/D=0.70 (location in between the pressure transducers).

6.3. Effect of out of plane velocity on pressure reconstruction

Once the general flow field has been described, it is possible to characterize the effect of the out-of-plane component on pressure estimation. From a mathematical point of view the inclusion of the out-of-plane velocity component (in a plane) only results in better estimation of the velocity magnitude (|V|), which appears in the denominator of equations 6 and 7.

To demonstrate the effect of the out-of-plane velocity component, Fig. 16 compares the pressure coefficient field for the two different PIV processing procedures, once again for Ma=0.8, α=0°. The

two PIV procedures consists in the stereo and planar PIV processing, with the latter obtained using only Camera 1 and Camera 3 (see the PIV setup in Fig. 3, right).

On the one hand, for the mean pressure coefficient no relevant variations are qualitatively distinguishable in the entire field of view (FOV). On the other hand, for the intensity of the pressure fluctuations, some differences arise in the separated area, with lower values of Cp_{std} for the planar-PIV based pressure field (Fig. 16, bottom). These differences may be connected with neglecting the out-of-plane velocity fluctuations, which are particularly intense in the boat tail separated area (see Fig. 14, bottom).

To further elucidate this aspect, Fig. 19 presents the average and standard deviation profiles of the Cp for the planar processing (see the profiles relative to the stereo processing in Fig. 17). The comparison of the average Cp profiles shows a slight increase in the discrepancy between the pressure transducers and the PIV-based procedure for the planar-PIV measurement. The standard deviation profiles confirm the previous observations, showing an underestimation of the fluctuation values, at all locations (x/D=0.25 and x/D=0.55 and x/D=0.85) for the planar PIV data. This mismatch is not surprising, since all the pressure transducers are located in the region where the fluctuations in the out-of-plane components are more intense.

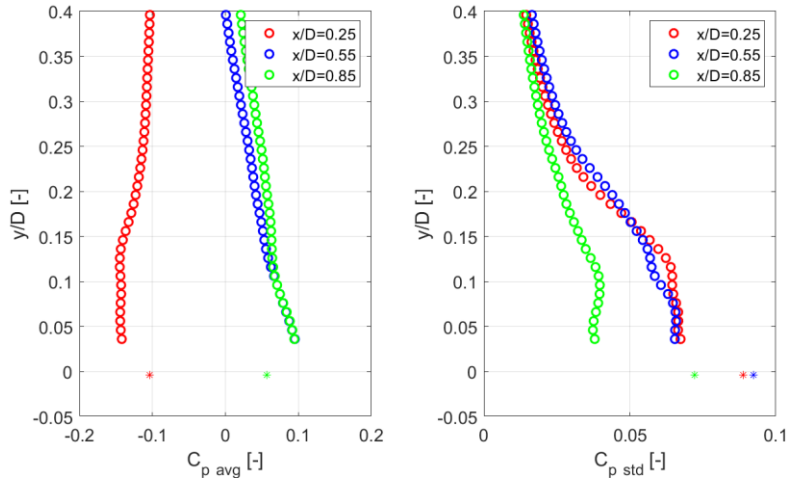

Figure. 19 Average (left) and standard deviation (right) of pressure coefficient profiles for Ma=0.8, α=0° for planar-PIV data.

7. Conclusions

This investigation successfully presented an approach to apply pressure from PIV to obtain unsteady pressure fluctuations around launcher configurations, particularly launcher fairings. The primary objective of developing a proven and validated methodology robust enough for application in industrial wind tunnel facilities was achieved.

Validation using synthetic data demonstrated the Taylor's hypothesis (TH) approach's good accuracy, with an average error in Cp estimation of approximately 0.02. Compared to an ideal Eulerian time-resolved approach, the TH approach showed a 5-10% increase in error.
In this study, for the first time, a single-snapshot approach (applying Taylor's hypothesis) was used to reconstruct pressure in experimental compressible conditions, showing excellent agreement with pressure transducers, as demonstrated for both instantaneous and mean pressure fields. The difference is minimal in terms of mean Cp value ($\Delta Cp_{avg} \approx 0.01$-$0.02$), though slightly larger in terms of the standard deviation of Cp ($\Delta Cp_{std} \approx 0.02$). This difference is not attributed to inaccuracies in the proposed pressure estimation but to the lack of velocity information in the small region close to the model surface, where high-energy fluctuations occur. This information is partially not captured from the selected FOV due to laser reflections and camera viewing angles.
Comparing the planar and stereo-PIV data in Section 6.3 has shown that including the out-of-plane velocity component (retrieved only with stereo-PIV measurements) in the pressure estimation does not significantly affect the mean pressure value and only provides some improvements in estimating pressure unsteadiness, particularly in the region of the fluctuating separated area.
In conclusion, the single snapshot method is a very attractive method for industrial compressible applications, where a complex PIV setup (e.g., dual-PIV or volumetric) or one restricted by technological limitations (e.g., time-resolved measurement in compressible conditions) is unfeasible.
The experimental PIV data revealed key flow features inherent in hammerhead geometry: two shockwave oscillation ranges, a separated area initiated in the boat tail region, and reattachment occurring at a distance of roughly 0.5D from the boat tail top corner. This distance is significantly reduced (by 0.3D) compared to the similar Coe and Nute geometry, mainly due to the smoother transition from the payload area to the boat tail region for the VEGA-E model (versus the sharp corner present in the Coe and Nute configuration).
The methodology used was capable of pinpointing regions of the launcher subjected to high unsteady loads, which are particularly relevant in the separated boat tail regions, with maximum values of Cp_{std} ($Cp_{std} \approx 0.09$) present for $0.1 < x/D < 0.6$. Interestingly, pressure unsteadiness due to the first shockwave oscillations are much less significant, with peak values of $Cp_{std} \approx 0.04$, while no relevant fluctuation in the secondary shockwave structure was observed.

Acknowledgments

This work has been carried out as part of the project TUPLE (Transonic PIV based unsteady pressure measurements for launcher environment), funded by the European Space Agency.

References

[1] Panda, J., Garbeff, T., Burnside, N., and Ross, J., "Unsteady pressure fluctuations measured on a hammerhead space vehicle and comparison with Coe and Nute's 1962 data," *International Journal of Aeroacoustics* 17, pp. 70–87, 2018.

[2] Schuster, D. M., Panda, J., Ross, J. C., Roozeboom, N. H., Burnside, N. J., Ngo, C. L., Sellers, M., and Powell, J. M., "Investigation of unsteady Pressure-Sensitive paint (uPSP) and a dynamic loads balance to predict launch vehicle buffet environments," *Tech. Rep. NASA/TM*-2016-219352, 2016.

[3] van Oudheusden, B.W., "PIV-based pressure measurement," *Measurement Science and Technology*, 24(032001), 2013.

[4] Pröbsting, S., Scarano, F., Bernardini, M., and Pirozzoli, S., "On the estimation of wall pressure coherence using time-resolved tomographic PIV," *Experiments in Fluids*, 54:1567, 2013.

[5] de Kat, R. and Ganapathisubramani, B., "Pressure from particle image velocimetry for convective flows: a Taylor's hypothesis approach," *Measurement Science and Technology*, 24(024002), 2013.

[6] McClure, J. and Yarusevych, S., "Optimization of planar PIV-based pressure estimates in laminar and turbulent wakes," *Experiments in Fluids*, 58:62, 2017.

[7] van Oudheusden, B.W., "Principles and application of velocimetry-based planar pressure imaging in compressible flows with shocks," *Experiments in Fluids*, 45:657–674, 2008.

[8] Scharnowski, S., and Kähler, C. J., "Investigation of a transonic separating/reattaching shear layer by means of PIV," *Theoretical and Applied Mechanics Letters*, 5(1):30–34, 2015.

[9] LaVision, "Flow Master Time-Resolved Particle Image Velocimetry Systems," *https://www.lavision.de/en/downloads/brochures.php*, 2017.

[10] Schreyer, A.M., Lasserre, J.J., and Dupont, P., "Development of a Dual-PIV System for High-Speed Flow Applications," *Experiments in Fluids* 56, 2015.

[11] Lynch, K.P., and Scarano, F., "Material acceleration estimation by four-pulse tomo-PIV," *Measurement Science and Technology*, 25(084005), 2014.

[12] van Oudheusden, B.W. and Souverein, L., "Evaluation of the pressure field from PIV in a shock wave boundary layer interaction," In *7th International Symposium on Particle Image Velocimetry*, Rome, Italy, 2007.

[13] Laskari, A., de Kat, R., and Ganapathisubramani, B., "Full-field pressure from snapshot and time-resolved volumetric PIV," *Experiments in Fluids*, 57:44, 2016.

[14] van Gent, P.L., Michaelis, D., van Oudheusden, B.W., Weiss, P.É., de Kat, R., Laskari, A., Jeon, Y.J., David, L., Schanz, D., Huhn, F., Gesemann, S., Novara, M., McPhaden, C., Neeteson, N.J., Rival,

D.E., Schneiders, J.F.G., and Schrijer, F.F.J., "Comparative assessment of pressure field reconstructions from particle image velocimetry measurements and Lagrangian particle tracking," *Experiments in Fluids*, 58:33, 2017.

[15] Lin, C., "On taylor's hypothesis and the acceleration terms in the Navier–Stokes equations," *Quarterly of Applied Mathematics*, 10(4):295–306, 1953.

[16] Davoust, S., and Jacquin, L., "Taylor's hypothesis convection velocities from mass conservation equation," *Physics of Fluids*, 23(5):051701, 2011.

[17] Van der Kindere, J. W., Laskari, A., Ganapathisubramani, B., and De Kat, R., "Pressure from 2D snapshot PIV," *Experiments in Fluids*, 60, 1-18, 2019.

[18] Souverein, L., van Oudheusden, B.W., and Scarano, F., "Particle image velocimetry based loads determination in supersonic flows," In *45th AIAA Aerospace Sciences Meeting and Exhibit*, AIAA Paper 2024-2145, 2007.

[19] Murai, Y., Nakada, T., Suzuki, T., and Yamamoto,. F., "Particle tracking velocimetry applied to estimate the pressure field around a Savonius turbine," *Measurement Science and Technology*, 18 2491–503, 2007.

[20] Charonko, J. J., King, C. V., Smith, B. L., and Vlachos, P. P., "Assessment of pressure field calculations from particle image velocimetry measurements," *Measurement Science and Technology*, 21(105401), 2010.

[21] de Kat, R., and van Oudheusden, B.W., "Instantaneous planar pressure determination from PIV in turbulent flow," *Experiments in Fluids*, 52(5):1089–1106, 2012.

[22] McClure, J., and Yarusevych, S., "Optimization of planar PIV-based pressure estimates in laminar and turbulent wakes," *Experiments in Fluids*, 58:62, 2017.

[23] Ragni, D., van Oudheusden, B.W., and Scarano, F., "Non-intrusive aerodynamic loads analysis of an aircraft propeller blade," *Experiments in Fluids*, 51, 2011.

[24] Coe, C.F., and Nute, J.B., "Steady and fluctuating pressures at transonic speeds on hammerhead launch vehicles," *Tech. rep. NASA TM X-778*, 1962.

[25] Goin, K. L., and Pope, A., "High-speed wind tunnel testing," New York, *John Wiley and sons INC*, p.320, 1965.

[26] Sciacchitano, A., and Scarano, F., "Elimination of PIV light reflections via a temporal high pass filter," *Measurement Science and Technology*, 25(8):084009, 2014.

[27] Ragni, D., Schrijer, F.F.J., van Oudheusden, B.W., and Scarano, F., "Particle tracer response across shocks measured by PIV," *Experiments in Fluids*, 50:53–64, 2011.

[28] D'Aguanno, A., Gonzalez Romero, A., Schrijer, F.F.J., and van Oudheusden, B.W., "Flow analysis of hammerhead launcher geometries in the transonic regime," In *AIAA SciTech Forum*, AIAA Paper 2024-2145, 2024.

[29] Schrijer, F.F.J., Sciacchitano, A., and Scarano, F., "Spatio-temporal and modal analysis of unsteady fluctuations in a high-subsonic base flow," *Physics of Fluids,* 26.8, 2014.

[30] Hudy, L. M., Naguib, A., Humphreys, W., and Bartram, S., "Particle image velocimetry measurements of a two/three-dimensional separating/reattaching boundary layer downstream of an axisymmetric backward-facing step," *43rd AIAA Aerospace Sciences Meeting and Exhibit*, AIAA Paper 2005-0114, 2005.